13.2

# FINSCALE STRUCTURE OF THE LAGRANGE, WYOMING, TORNADO DURING VORTEX2: GBVTD AND PHOTOGRAMMETRIC ANALYSES

Phillip Stauffer*[1], Roger M. Wakimoto[1], Wen-Chau Lee[1], Nolan T. Atkins[2], Joshua Wurman[3]

[1]*National Center for Atmospheric Research, Boulder, Colorado*
[2]*Department of Atmospheric Sciences, Lyndon State College, Lyndonville, Vermont*
[3]*Center for Severe Weather Research, Boulder, Colorado*

## 1. INTRODUCTION

Radar, and more recently mobile radar, has allowed detailed studies of high-resolution reflectivity and velocity data of the hook echo, mesocyclone, and the tornadic-vortex signature (e.g. Stout and Huff 1953; Brown et al. 1978; Zrnic and Istok 1980; Forbes 1981; Bluestein et al. 1993,1997, 2004,2007a,b; Wurman et al 1996; Wurman and Gill 2000; Burgess et al. 2002; Alexander and Wurman 2005; Wurman et al. 2007a). Dual Doppler analyses have been accomplished with radars deployed approximately 7-10 km from the tornadic circulation, resulting in the data being interpolated to a Cartesian grid with 100 m grid-spacing (e.g., Wurman et al. 2007a,b, 2010a; Marquis et al. 2008). These dual Doppler analyses are limited, by being unable to fully resolve the tornado circulation unless it is 1 km or larger (e.g. Carbone et al. 1985). Thus, the use of other techniques to utilize the finescale single Doppler velocities to retrieve the three-dimensional tornado wind field has increased in popularity. One such technique, which appears to hold the most promise, is the ground-based velocity track display technique (GBVTD; Lee et al. 1999) using a decomposition similar to the velocity azimuth display (VAD; Browning and Wexler 1968). Past studies have used the GBVTD analysis to resolve the two-dimensional (Bluestein et al. 2003, 2007a; Tanamachi et al. 2007) and the three-dimensional (Lee and Wurman 2005; Kosiba and Wurman 2010) wind field of the tornado circulation.

Photographs and video documenting the life cycle of the tornado are fairly common. Detailed photogrammetric analyses, co-located with the radar, of tornadoes have been relatively rare (Bluestein et al. 1993, 1997, 2004, 2007a,b; Tanamachi et al. 2007, Wakimoto et al. 2003). Wakimoto and Martner (1992) provided a photogrammetric and Doppler radar analysis of the entire life cycle of a nonsupercell tornado.

The June 5, LaGrange, Wyoming, tornado was sampled by the Doppler-on-Wheels (DOWs; Wurman et al. 1997; Wurman 2001) during the Second Verification of the Origins of Rotation in Tornadoes Experiment (VORTEX2). This event provided a unique opportunity to assess the GBVTD technique with the dual-Doppler retrieved wind fields and compare the visual features of the funnel cloud with the GBVTD retrieved fields.

## 2. DOW radars and photogrammetry

The radar data used in this study were collected by DOW6 and DOW7. The DOWs are 3-cm wavelength radars mounted on trucks to collect data near tornadoes. Additional information about the DOWs can be obtained from Wurman et al. (1997) and Wurman (2001). The dual-Doppler coordinated volume scans were performed every two minutes at the elevation scans (0.5°, 1°, 2°, 3°, 4°, 5°, 6°, 8°, 10°, 12°, 14°, and 16°) to sample the tornado structure. The radar reflectivity and Doppler velocity data values for DOW7 were calibrated to within ±2 dBZ and 1 m $s^{-1}$, respectively. The data for DOW6 and DOW7 were navigated using ground clutter targets as well as edited and de-aliased using the SOLO software (Oye et al. 1995).

Photogrammetric analysis allows quantitative information to be derived from photographs of tornadoes (e.g. Malkus 1952; Rasmussen et al. 2003; Zehnder et al. 2007). An overview of photogrammetry can be found in Abrams (1952) and Holle (1986). Determining the location of the camera and the azimuth angles of several targets identified in the horizon shown in the picture is the necessary first step. Subsequently, the effective focal length and tilt angle of the camera can be

* *Corresponding Author Address:* Phillip Stauffer
NCAR, P.O. Box 3000, Boulder, CO 80307

found using spherical trigonometry. These parameters are then used to construct an elevation- and azimuth-angle grid to be superimposed on top of the photograph. Comparison of the computed azimuths with the know location of targets, suggests that the accuracy is good with azimuth angle errors in the range of 0.1° and 0.2°. Additional details of the technique used to analyze the photos in this study are presented in Wakimoto et al. (2011).

**3. GBVTD and Dual Doppler**

The GBVTD methodology was formulated in Lee et al. (1999). This technique assumes that the circulation is characterized by a quasi-axisymmetric structure. Several steps are performed to create a GBVTD analysis. The radar data are adjusted to a common time using an advection correction based on the mesocyclone motion (12 m $s^{-1}$ from 275°) and the tornado motion is subtracted from the radial wind fields. Then the radial velocities are interpolated onto a Cartesian grid using a bilinear interpolation algorithm. A series of analysis rings are centered on the circulation at different radii, after the center of the circulation has been objectively located for each height level using a methodology outlined in Lee and Marks (2000). A least squares fit of the radial velocity data at each radius is applied, up to angular wavenumber 3. This acts as a filter and removes higher order wavenumber artifacts that may have been created by the bilinear interpolation.

Lee et al. (1999) illustrate, using Fourier decomposition, how the axisymmetric tangential and radial velocities result in a simple sine curve with a phase shift. Asymmetric circulations are composed of mean flow and waves of all forms, where the complex waveform can be decomposed into Fourier components. This system however is underdetermined and not all of the Fourier coefficients can be uniquely determined. $V_RC_n$ and $V_TC_n$ ($V_RS_n$ and $V_TS_n$) are defined as the amplitude of the cosine (sine) components of the tangential ($V_T$) and radial velocity ($V_R$), respectively, for angular wavenumber n (hereafter, angular wavenumber is refereed to as wavenumber). Lee et al. (1999) has shown that the axisymmetric tangential and radial velocity can be represented by the following equations:

$$V_TC_0 = -B_1 - B_3 - V_M \sin(\theta_T - \theta_M)\sin\alpha_{\max} + V_RS_2 \quad (1)$$

$$V_RC_0 = A_1 + A_3 - V_RC_2 \quad (2)$$

where $V_M$ represents the mean flow; and $A_1$, $A_3$, $B_1$, and $B_3$ are the Fourier coefficients for wavenumbers 1 and 3 of the Doppler velocities analyzed on each radius. The basic geometry for the GBVTD analysis is shown in Fig. 1.

The closure assumption proposed by Lee et al. (1994) states that the asymmetric radial velocity was much smaller than the corresponding tangential velocity. As a result the higher order $V_RS_2$ and $V_RC_2$ terms are neglected in (1) and (2), respectively. It was also assumed that the perpendicular component of the mean flow (which is also perpendicular to the single Doppler radar beam and unobservable), $V_M(\theta_T-\theta_M)$, was small compared to the other terms. The end products of this procedure are the axisymmetric mean (hereafter referred to as the mean) radial and tangential winds and asymmetric tangential winds for each level. From these winds the mean divergence, vertical velocity (computed from an upward integration of divergence), vertical vorticity, and angular momentum can be computed. The perturbation pressure gradient associated with the primary circulation can also be determined.

The Dual-Doppler wind syntheses based on the DOW6 and DOW7 radars were available and allow a direct estimate of the ignored terms in (1) and (2). The radar data were interpolated onto a Cartesian grid using an objective analysis two-pass Barnes filter. The data were adjusted to a common time using an advection correction. The multipass analysis has been shown to result in less damping at well-resolved wavelengths while suppressing small-scale noise (Majcen et al. 2008). The maximum horizontal data spacing ($\delta$) was 244m due to the oversampling in the azimuthal direction. The resultant smoothing parameter was 0.106 $km^2$ (Pauley and Wu 1990). The horizontal and vertical grid spacing was 100m ($\delta$/2.5; Koch et al. 1983). The vertical velocities were derived from an upward integration of the continuity equation.

The range-height profiles of the azimuthally averaged dual-Doppler $V_R$, the DOW7 GBVTD analysis of $V_R$ ignoring the $V_RC_2$ term, the DOW7 GBVTD $V_R$ with the $V_RC_2$ , and the DOW6 GBVTD $V_R$ with the $V_RC_2$ term is presented in Fig. 2 panels a,b,c, and d, respectively. The $V_RC_2$ term was estimated from the dual-Doppler wind synthesis as a proxy. The GBVTD analyses have been filtered to match the resolvable scales of the dual-Doppler wind synthesis. There are striking differences between the GBVTD estimate of $V_R$ and the dual-Doppler wind synthesis. The GBVTD analysis including the $V_RC_2$ term largely replicate the main features that are apparent in Fig. 2a. The stronger GBVTD $V_R$ values are a result of the high resolution data collected by the DOW7 radar. Comparison of the DOW6 $V_R$ including the $V_RC_2$ with the dual-Doppler $V_R$ shows broad similarities, but the agreement is not as good. These differences are likely the result of the greater distance between the DOW6 site and the tornado.

These profiles of $V_R$ show that the axisymmetric radial velocities are not significantly larger than the asymmetric radial velocities, and the closure assumptions discussed by Lee et al. (1999) are not valid for this case. From (1) and (2), the unresolved wavenumber-2 radial wind component directly biases the mean tangential and radial winds of the vortex. The closure assumption is appropriate in stronger tornadoes (e.g. Lee and Wurman 2005). The other unresolved terms were also assessed in (2) and the GBVTD $V_T$ and dual-Doppler $V_T$ were in close agreement (not shown). For the GBVTD results presented here, the $V_R$ included the $V_RC_2$ term and the $V_T$ was computed using the simplified version (ignoring $V_M$ and $V_RS_2$).

## 4. GBVTD analysis of the LaGrange Tornado

GBVTD analyses were performed during the 2216 and 2218 UTC volume scans by the DOW7 radar. The distance of the tornado at these times was approximately 5.5 and 3.6 km from DOW7. These distances were deemed close enough to reconstruct the tornado circulation using the GBVTD technique. The initial deployment of DOW6 and DOW7 on the LaGrange supercell is shown in Fig. 3. The characteristics of the hook echo starting with the initial intensification until a few minutes before dissipation are also shown. To take advantage of the high resolution single Doppler velocity data, the grid spacing for the GBVTD analysis was 50 m in the vertical for both volume times while the horizontal was 50 m and 40 m for the 2216 and 2218 UTC volumes, respectively.

### a. 2216:08 – 2216:45 UTC Volume

A vertical cross section of radar reflectivity and the two-dimensional vertical and radial wind field derived from the GBVTD analysis through the center of the tornado is shown in Fig 4a. Centered on the tornado there is a weak echo hole (WEH; Fujita 1981), shaded blue, resulting from centrifuging of hydrometeors (Dowell et al. 2005) and is associated with a larger diameter than the visible funnel. Small debris particles being lofted from the surface are resulting in higher (>45 dBZ) echoes beneath the WEH (Wakimoto et al. 2011). The prominent axial downdraft in the wind field has also been noted by other investigators (e.g. Wurman and Gill 2000; Lee and Wurman 2005; Kosiba et al. 2008; Kosiba and Wurman 2010). The GBVTD analysis does not extent to the center of the tornado due to the lack of data points at small radii needed to resolve the wave (Carbone et al. 1985).

The downdraft is largely confined within the condensation funnel and has speeds exceeding 24 m $s^{-1}$ (Fig. 4b). The maximum updraft is just above the surface at 4 m $s^{-1}$ and is located at the periphery of the funnel. This suggests a two-celled structure (e.g. Davies-Jones 1986). In response to the axial downdraft, there is strong low-level outflow in the mean radial velocities near the surface (Fig. 4c). Shallow inflow is confined to a small region outside the tornado core.

The mean tangential velocities are shown in Fig. 4d, and have maximum speeds in excess of 50 m $s^{-1}$ near the surface. DOW7 is not resolving the expected frictional decrease in the tangential velocities within the surface layer. The existence of strong rotation near the ground suggests that a downward directed perturbation pressure (hereafter, perturbation pressure is referred to as pressure) gradient exists. Using the equation outlined in Lee and Wurman (2005) the pressure field (Fig. 4e) was calculated at each height independently, assuming that all perturbations at 3-km radius are zero. The pressure gradient should be interpreted with caution (e.g. Gal-Chen 1978), however all plots of pressure deficits with radius (not shown) reveal no change in pressure beyond a radius of 1 km. A surface-based mesolow (<-30 mb) is evident, and results in a very strong vertical pressure gradient. This is consistent with the existence of the axial downdraft.

The maximum vertical vorticity values are greater than 45 X $10^{-2}$ $s^{-1}$ within the tornado core (Fig. 4f) and the vertical vorticity quickly approaches zero outside the tornado funnel. The angular momentum (Fig. 4g) is relatively constant with height near and within the radius of maximum winds as noted by Lee and Wurman (2005), Rasmussen and Straka (2007), Kosiba et al. (2008), and Kosiba and Wurman (2010) and is similar to the axisymmetric profiles associated with hurricanes (e.g. Lee et al. 2000), as well as high resolution simulations of tornadoes (e.g. Lewellen et al. 2000). The angular momentum increases radially outward with the strongest gradient within and just beyond the visible funnel. The dashed isopleths near the surface represent the low angular momentum flow that should exist, but is not being detected by DOW7. With the strong outflow of the winds near the surface, as well as weaker outflow throughout the region, the angular momentum is being advected away from the tornado. It would be expected that the LaGrange tornado will weaken with time [this is consistent with the results shown by Atkins et al. (2012)]. This possible trend will be assessed in the next section.

**b. 2218:07 – 2218:42 UTC Volume**

The axial downdraft increased in intensity during the 2218 UTC volume scan, but is weaker at low levels (Figs. 5a, b). This stronger downdraft can partially be attributed to the ability to resolve the wind field closer to the tornado center as the tornado approached the DOW7 site. The updrafts, at low levels, are still confined to the periphery of the funnel, but are weaker than the previous volume analysis. The radial inflow strength and radial extent has increased (Figs. 5a, c) near the surface. This increase and extent could be due to Doppler velocities being collected closer to the ground during this time owing to the lower beam height and smaller beamwidth. The vertical velocity fields derived from GBVTD technique should be viewed with caution, since the divergence fields at the lower boundary may not be fully resolved.

The angular momentum being advected away from the tornado during the 2216 volume suggests that the circulation may be weakening. Indeed, the tangential velocities have decreased at all levels (Fig. 5d). The azimuthal shear computed from raw single Doppler velocities shows a decrease in intensity at this time (Fig. 6). There is also a weaker downward-directed pressure gradient (Fig. 5e) within the surface mesolow owing to the weaker rotational speeds. Interestingly, the vertical vorticity has increased to >55 X $10^{-2}$ $s^{-1}$ (Fig. 5f). This increase is likely due to the GBVTD analysis resolving larger vorticity values closer to the tornado center than the previous analysis time. The tornado circulation is contracting at this time, as evident from single Doppler velocity data (not shown). The contraction of the circulation in a diffluent wind field at low levels appears to be contradictory. However, it is believed that centrifuging of hydrometeors is masking low-level confluent winds into the tornado.

Another way to assess the overall trend is to compare the values observed at the earlier analysis with the current analysis time. A few isopleths (light blue dashed lines) from the previous time are plotted near the funnel and illustrate that the vertical vorticity has increased slightly at most heights. While the increase appears to be inconsistent with the observed weakening of the tangential velocities and azimuth shear, the increase was found to be due to an increase in the shear vorticity even though the curvature vorticity weakens. A similar comparison with the angular momentum fields (Fig. 5g), however, shows that overall the angular momentum has decreased from the previous analysis time within the tornado core. Comparing the wind fields, the 2218 UTC analysis is more diffluent and continues to support angular momentum being advected away from the tornado. The LaGrange tornado dissipated at ~2230 UTC.

## 5. Low-level convergence and centrifuging of hydrometeors

While mobile Doppler radars have collected unprecedented high-resolution data of tornadoes, it still remains a challenge to collect information at the lowest tens of meters. These lowest levels are where the strongest radial inflow would be expected (e.g. Lewellen et al. 1997). In addition, the convergence signal at low levels could be masked by the centrifuging of hydrometeors/debris within the tornado core (e.g. Snow 1984; Wurman and Gill 2000; Dowell et al. 2005). The impact of the centrifuging of hydrometeors is schematically illustrated in Fig. 7, where the path of the hydrometeors is different than the air. There is net trajectory outward from the tornado; this centrifuging contributes to the formation of the WEH and biases the Doppler velocities with a false divergent signature (i.e. a positive bias to the radial velocity measurements). Figure 8 attempts to summarize the difficulty of accurately measuring the low-level inflow into the tornado. This difficulty is due to the centrifuging of hydrometeors/debris and the inability of the radar beam to fully resolve the inflow, which is confined to the lowest levels.

Centrifuging effect estimates have been provided by past investigations and suggested it could be important (Wurman and Gill 2000; Dowell et al. 2005). The large radius of maximum wind and strong radial inflow for the Mulhall tornado would have largely negated the impact of centrifuging, as suggested by Lee and Wurman (2005) and would have resulted in a “minor shift of the overall pattern”. Concerned that centrifuging of debris had contaminated the radial velocities; Rasmussen and Straka (2007) did not incorporate data close to the center of the tornado when calculating angular momentum. The LaGrange tornado was not violent (EF2) and was characterized by a small radius of maximum wind and weak radial inflow. As a result, the wind profiles, associated with this type of tornado, could be strongly influenced by the centrifuging of hydrometeors.

To estimate the effect of centrifuging for this study, the approach outlined by Dowell et al (2005) was followed. All the assumptions made in Dowell et al. (2005) were retained, however to simplify the estimates of the centrifuging, the effect of small debris particles was ignored and it was assumed that radar reflectivity returns were only from hydrometeors. Polarimetric observations have proven to be particularly useful (e.g. Ryzhkov et al. 2005; Bluestein et al. 2007b) in discriminating hydrometeor types, however, the polarimetric observations were not suitable for this study. The median volume diameter ($D_0$) was computed from the radar reflectivity profile based on a Marshall-Palmer size distribution (Marshall and Palmer 1948), and was assumed $D_0$ represents the drop size in the sampling volume. The terminal velocity can be estimated based on the known drop size (Atlas et al. 1973). The drops were initially assumed to move with the same horizontal mean GBVTD velocities as the air, such that the particle motions are determined by the forcing rather than by the initialization. The results presented are after sufficient time had elapsed such that the particle motions have asymptotically approached the steady solutions.

Plotted in Figs. 9a, b, are the 2216 and 2218 UTC estimates of the positive bias to the radial velocities due to the centrifuging, respectively. For both analysis times the centrifuging effect is similar. The impact is the largest at low levels where the tangential velocities are the strongest and closest to the tornado core. A sensitivity analysis using a uniform reflectivity profile instead and repeating the particle motion calculations, exhibited similar results. The particle radial velocities depicted in Fig. 9 are of the same order of magnitude as the radial velocities shown in Figs. 4c and 5c and suggest there is a significant impact on the divergence field, especially at low levels. The measured radial velocity profiles were then corrected for the particle motions by subtracting the two fields, after which the divergence was recomputed. The new vertical velocity field, with the particle motion correction applied, show striking differences (Figs. 10 and 11) with the plots shown in Figs. 4b and 5b. The axial downdraft for the 2216 UTC volume is absent (Figs. 10a and 11a). There are downdrafts confined to the lowest few hundred meters, while updrafts exist at higher levels. Near the surface the radial outflow strength has been reduced. The corrected 2218 UTC volume is also different than the early time. Stronger radial inflow supports low-level updrafts within the tornado core (Figs 10b and 11b) and weak axial downdrafts exist aloft. The effect of particle motion on the mean tangential velocities, vertical vorticity, and angular momentum was negligible (not shown).

The results suggest that Doppler radar data collected on tornadoes associated with a small radius of maximum wind and relatively weaker radial inflow could be significantly biased owing to particle centrifuging. The estimates should be view with caution and are subject to the assumptions stated earlier. After the correction was applied to this case the radial and vertical velocity fields within the tornado core were significantly altered.

Resolving the low-level inflow is critical for correctly setting the lower boundary condition for vertical velocity calculations. The increase in the low-level radial inflow (Figs. 4c and 5c) may be due to the natural tornado evolution or it is possible that the radar was better able to resolve the low-level inflow as the tornado approached. The author's have concluded that the latter is the more likely scenario, since the radar beamwidth decreases by more than 50%, at the distance of the tornado, between the two volume scans. Therefore, we recommend that the radar be deployed within a few kilometers from the tornado or that other high-resolution platforms be used such as W- or K-band radar (e.g. Bluestein et al. 2007a) or a lidar (e.g. Bluestein et al. 2010).

**6. Summary and discussion**

The current study presents a GBVTD radar analysis combined with photography of the LaGrange, Wyoming, tornado on 5 June 2009 during VORTEX2. The three-dimensional wind field of the tornadic circulation was reconstructed for two volume scans, where the funnel was within a few kilometers of the Doppler radar. A strong axial downdraft was evident and supported by a downward-directed pressure gradient. The weak radial inflow was apparent and attributed to a combination of centrifuging of hydrometeors/debris in the tornado and the inability of the radar to resolve the low-level flow. The maximum tangential velocities were confined to the surface and were >50 m $s^{-1}$. There was an intense column of vertical vorticity associated with the tornado, which rapidly weakened outward. Advection of angular momentum was away from the circulation, consistent with the weakening of the tornado during the analysis period.

The assumptions in the GBVTD methodology were assessed due to the availability of a dual-Doppler wind synthesis. The analysis suggests that the neglected higher-order terms be retained in the presence of weak radial inflow, to retrieve the most accurate wind field. The quantitative analysis of centrifuging of hydrometeors/debris suggests that the radial and vertical velocity profile can be significantly altered for intense circulations with a small radius of maximum wind and relatively weaker inflow.

The analysis of the LaGrange tornado highlights the difficulty of achieving high-resolution dual-Doppler wind synthesis of tornadic wind fields. Techniques such as the GBVTD will need to be applied along with remote sensing techniques that are better able to resolve the low-level inflow into the tornado. Polarimetric data will also be important to assess the hydrometeor type and the location of debris in removing possible contamination of the Doppler velocity data. Future studies will, hopefully, be able to apply the techniques illustrated in this paper on tornadoes of different intensity and widths and also for a longer period of the tornado's life cycle. These additional analyses will also be needed to verify the results shown in this paper, which were restricted to two radar volume scans.

*Acknowledgments*. Any opinion, findings, conclusions, or recommendations expressed in this publication are those of the authors and do not necessarily reflect the views of the National Science Foundation. The authors wish to thank David Dowell who provided several helpful suggestions for calculating the particle motion. Research results presented in this paper were supported by the National Science Foundation under Grant ATM-0757714. The DOW radars are National Science Foundation Lower Atmospheric Observing Facilities supported by Grant ATM-0734001. The DOW deployments in VORTEX2 have been supported by Grants ATM-0910737 and ATM-0966095. Analysis of DOW data has been supported by Grant ATM-0947235. VORTEX2 has been supported, in part, by Grant ATM-0724318.

**REFERENCES**

Abrams, T., 1952: The Manual of Photogrammetry. George Banta Publishing, 876 pp.

Alexander, C. R., and J. Wurman, 2005: The 30 May 1998 Spencer, South Dakota, storm. Part I: The structural evolution and environment of the tornadoes. Mon. Wea. Rev., 133, 72–96.

Atkins, N. T., A. McGee, R. Ducharme, R. M. Wakimoto, and J. Wurman, 2012: The LaGrange tornado during VORTEX2. Part II: Photogrammetric analysis of the tornado combined with dual-Doppler radar data. Mon. Wea. Rev., in press.

Atlas, D., R. C. Srivastava, and R. S. Sekhon, 1973: Doppler radar characteristics of precipitation at vertical incidence. Rev. Geophys. Space Phys., 2, 1–35.

Bluestein, H. B., 1999: A history of severe-storm-intercept field programs. Wea. Forecasting, 14, 558–577.

——, J. G. LaDue, H. Stein, D. Speheger, and W. P. Unruh, 1993: Doppler radar wind spectra of supercell tornadoes. Mon. Wea. Rev., 121, 2200–2221.

——,W. P.Unruh,D.C.Dowell, T.A.Hutchinson, T.M. Crawford, A. C. Wood, and H. Stein, 1997: Doppler radar analysis of the Northfield, Texas, tornado of 25 May 1994. Mon. Wea. Rev.,125, 212–230.

——, W.-C. Lee, M. Bell, C. C. Weiss, and A. L. Pazmany, 2003: Mobile Doppler radar observations of a tornado in a supercell near Bassett, Nebraska, on 5 June 1999. Part II: Tornadovortex structure. Mon. Wea. Rev., 131, 2968–2984.

——, C. C.Weiss, andA. L. Pazmany, 2004: The vertical structure of a tornado near Happy, Texas, on 5 May 2002: High-resolution, mobile,W-band, Doppler radar observations.Mon. Wea. Rev., 132, 2325–2337.

——, ——, M. M. French, E. M. Holthaus, R. L. Tanamachi, S. Frasier, andA. L. Pazmany, 2007a: The structure of tornadoes near Attica, Kansas, on 12 May 2004: High- resolution, mobile, Doppler radar observations. Mon. Wea. Rev., 135, 475–506.

——, M. M. French, R. L. Tanamachi, S. Frazier, K. Hardwick, F. Junyent, and A. L. Pazmany, 2007b: Close range observations of tornadoes in supercells made with a dual-polarization, X-band, mobile Doppler radar. Mon. Wea. Rev., 135, 1522–1543.

——, and Coauthors, 2010: A summary of data collected during VORTEX2 by MWR-05XP/TWOLF, UMASS X- pol, and the UMASS W-band radar. Preprints, 25th Conf. on Severe Local Storms, Denver, CO, Amer. Meteor. Soc., P5.4. [Available online at https://ams.confex.com/ams/pdfpapers/176197.pdf.]

Brown, R. A., L. R. Lemon, and D. W. Burgess, 1978: Tornado detection by pulsed Doppler radar.Mon. Wea. Rev., 106, 29–38.

Browning, K. A., and R. Wexler, 1968: The determination of kinematic properties of a wind field using Doppler radar. J. Appl. Meteor., 7, 105–113.

Burgess, D. W., M. A. Magsig, J. Wurman, D. C. Dowell, and Y. Richardson, 2002: Radar observations of the 3 May 1999 Oklahoma City tornado. Wea. Forecasting, 17, 456–471.

Carbone, R. E., M. J. Carpenter, and C. D. Burghart, 1985: Doppler radar sampling limitations in convective storms. J. Atmos. Oceanic Technol., 2, 357–361.

Davies-Jones, R. P., 1986: Tornado dynamics. Thunderstorms: A Social, Scientific and Technological Documentary, Vol. 2, Thunderstorm Morphology and Dynamics, E. Kessler, Ed., University of Oklahoma Press, 197–236.

Dowell, D. C., C. R. Alexander, J. M. Wurman, and L. J. Wicker, 2005: Centrifuging of hydrometeors and debris in tornadoes: Radar reflectivity patterns and wind-measurement errors. Mon. Wea. Rev., 133, 1501–1524.

Forbes, G. S., 1981: On the reliability of hook echoes as

tornado indicators. Mon. Wea. Rev., 109, 1457–1466.
Fujita, T. T., 1981: Tornadoes and downbursts in the context of generalized planetary scales. J. Atmos. Sci., 38, 1511–1534.
Gal-Chen, T., 1978: A method for the initialization of the anelastic equations for matching models with observations. Mon. Wea. Rev., 106, 587–606.
Holle, R. L., 1986: Photogrammetry of thunderstorms. Thunderstorms: A Social and Technological Documentary, Vol. 3, Thunderstorm Morphology and Dynamics, E. Kessler, Ed., University of Oklahoma Press, 77–98.
Koch, S. E., M. desJardins, and P. J. Kocin, 1983: An Interactive Barnes objective map analysis scheme for use with satellite and conventional data. J. Climate Appl. Meteor., 22, 1487–1503.
Kosiba, K., and J. Wurman, 2010: The three-dimensional axisymmetric wind field structure of the Spencer, South Dakota, 1998 tornado. J. Atmos. Sci., 67, 3074– 3083.
——, R. J. Trapp, and J. Wurman, 2008: An analysis of the axisymmetric three-dimensional low level wind field in a tornado using mobile radar observations. Geophys. Res. Lett., 35, L05805, doi:10.1029/2007GL031851.
Lee, W.-C., and F. D. Marks, 2000: Tropical cyclone kinematic structure retrieved from single Doppler radar observations. Part II: The GBVTD-simplex center finding algorithm. Mon. Wea. Rev., 128, 1925–1936.
——, and J. Wurman, 2005: Diagnosed three-dimensional axisymmetric structure of the Mulhall tornado on 3 May 1999. J. Atmos. Sci., 62, 2373–2393.
——, F. D. Marks, and R. E. Carbone, 1994: Velocity track display— A technique to extract real-time tropical cyclone circulations using a single airborne Doppler radar. J. Atmos. Oceanic Technol., 11, 337–356.
——, B. J.-D. Jou, P.-L. Chang, and S.-M. Deng, 1999: Tropical cyclone kinematic structure retrieved from single-Doppler radar observations. Part I: Interpretation of Doppler velocity patterns and the GBVTD technique. Mon. Wea. Rev., 127, 2419–2439.
——,——,——, and F. D.Marks, 2000: Tropical cyclone kinematic structure retrieved from single-Doppler radar observations. Part III: Evolution and structure of TyphoonAlex (1987).Mon. Wea. Rev., 128, 3982–4001.
Lewellen, D. C., and W. S. Lewellen, 2007a: Near surface intensification of tornado vortices. J. Atmos. Sci., 64, 2176–2194.
——, and ——, 2007b: Near-surface vortex Intensification through corner flow collapse. J. Atmos. Sci., 64, 2195– 2209.
——, ——, and J. Xia, 2000: The influence of a local swirl ratio on tornado intensification near the surface. J. Atmos. Sci., 57, 527–544.
Lewellen, W. S., D. C. Lewellen, and R. I. Sykes, 1997: Large eddy simulation of a tornado's interaction with the surface. J. Atmos. Sci., 54, 581–605.
Majcen, M., P. Markowski, Y. Richardson, D. Dowell, and J. Wurman, 2008: Multipass objective analyses of Doppler radar data. J. Atmos. Oceanic Technol., 25, 1845–1858.
Malkus, J., 1952: The slopes of cumulus clouds in relation to external wind shear. Quart. J. Roy. Meteor. Soc., 78, 530–542.
Marquis, J., Y. Richardson, J. Wurman, and P. Markowski, 2008: Single- and dual-Doppler analysis of a tornadic vortex and surrounding storm-scale flow in the Crowell, Texas, supercell of 30 April 2000. Mon. Wea. Rev., 136, 5017–5043.
Marshall, J. S., and W. Palmer, 1948: The distribution of raindrops with size. J. Meteor., 5, 165–166.
Oye, R., C. Mueller, and S. Smith, 1995: Software for radar translation, visualization, editing, and Interpolation. Preprints, 27th Conf. on Radar Meteorology, Vail, CO, Amer. Meteor. Soc., 359–361.
Pauley, P. M., and X. Wu, 1990: The theoretical, discrete, and actual response of the Barnes objective analysis scheme for one- and two-dimensional fields. Mon. Wea. Rev., 118, 1145–1163.
Rasmussen, E. N., and J. M. Straka, 2007: Evolution of low-level angular momentum in the 2 June 1995 Dimmitt, Texas, tornado cyclone. J. Atmos. Sci., 64, 1365–1378.
——, R. Davies-Jones, and R. L. Holle, 2003: Terrestrial photogrammetry of weather images acquired in uncontrolled circumstances. J. Atmos. Oceanic Technol., 20, 1790–1803.
Ryzhkov, A. V., T. J. Schuur, D. W. Burgess, and D. S. Zrnic, 2005: Polarimetric tornado detection. J. Appl. Meteor., 44, 557–570.
Snow, J. T., 1984: On the formation of particle sheaths in columnar vortices. J. Atmos. Sci., 41, 2477–2491.
Stout, G. E., and F. A. Huff, 1953: Radar records Illinois tornadogenesis. Bull. Amer. Meteor. Soc., 34, 281–284.
Tanamachi, R. L., H. B. Bluestein, W.-C. Lee, M. Bell, and A. Pazmany, 2007: Ground-based velocity track display (GBVTD) analysis of W-band Doppler radar data in a tornado near Stockton, Kansas, on 15 May 1999. Mon. Wea. Rev., 135, 783–800.
Wakimoto, R. M., and B. E. Martner, 1992: Observations of a Colorado tornado. Part II: Combined photogrammetric and Doppler radar analysis. Mon. Wea. Rev., 120, 522–543.
——, H. V. Murphey, D. C. Dowell, and H. B. Bluestein, 2003: The Kellerville tornado during VORTEX: Damage survey and Doppler radar analyses. Mon. Wea. Rev., 131, 2197–2221.
——, N. T. Atkins, and J. Wurman, 2011: The LaGrange tornado during VORTEX2. Part I: Photogrammetric analysis of the tornado combined with single-Doppler radar data. Mon. Wea. Rev., 139, 2233–2258.
Wurman, J., 2001: The DOW mobile multiple-Doppler network. Preprints, 30th Int. Conf. on Radar Meteorology, Munich, Germany, Amer. Meteor. Soc.,

P3.3. [Available online at https://ams.confex.com/ams/30radar/techprogram/paper_21572.htm.]

——, and S. Gill, 2000: Finescale radar observations of t heDimmitt, Texas (2 June 1995), tornado. Mon. Wea. Rev., 128, 2135–2164.

——, J. M. Straka, and E. N. Rasmussen, 1996: Fine-scale Doppler radar observations of tornadoes. Science, 272, 1774–1777.

——, ——, ——, M. Randall, and A. Zahrai, 1997: Design and deployment of a portable, pencil-beam pulsed 3- cm Doppler radar. J. Atmos. Oceanic Technol., 14, 1502–1512.

——, Y. Richardson, C. Alexander, S. Weygandt, and P. F. Zhang, 2007a: Dual-Doppler and single-Doppler analysis of a tornadic storm undergoing mergers and repeated tornadogenesis. Mon. Wea. Rev., 135, 736–758.

——, ——, ——, ——, and ——, 2007b: Dual-Doppler analysis of winds and vorticity budget terms near a tornado. Mon. Wea. Rev., 135, 2392–2405.

——, P. Robinson, C. Alexander, and Y. Richardson, 2007c: Low-level winds in tornadoes and potential catastrophic tornado impacts in urban areas. Bull. Amer. Meteor. Soc., 88, 31–46.

——, K. Kosiba, P. Markowski, Y. Richardson, D. Dowell, and P. Robinson, 2010a: Finescale single- and dual- Doppler analysis of tornado intensification, maintenance, and dissipation in the Orleans, Nebraska, supercell. Mon. Wea. Rev., 138, 4439–4455.

——, L. J. Wicker, Y. P. Richardson, E. N. Rasmussen, P. M. Markowski, D. Dowell, D. W. Burgess, and H. B. Bluestein, 2010b: An overview of the VORTEX2 field campaign. Preprints, 25th Conf. on Severe Local Storms, Denver, CO, Amer. Meteor. Soc., 5.1. [Available online at https://ams.confex.com/ams/25SLS/techprogram/paper_176068.htm.]

Zehnder, J. A., J. Hu, and A. Razdan, 2007: A stereo photogrammetric technique applied to orographic convection. Mon. Wea. Rev., 135, 2265–2277.

Zrnic, D., and M. Istok, 1980: Wind speeds in two tornadic storms and a tornado, deduced from Doppler spectra. J. Appl. Meteor., 19, 1405–1415.

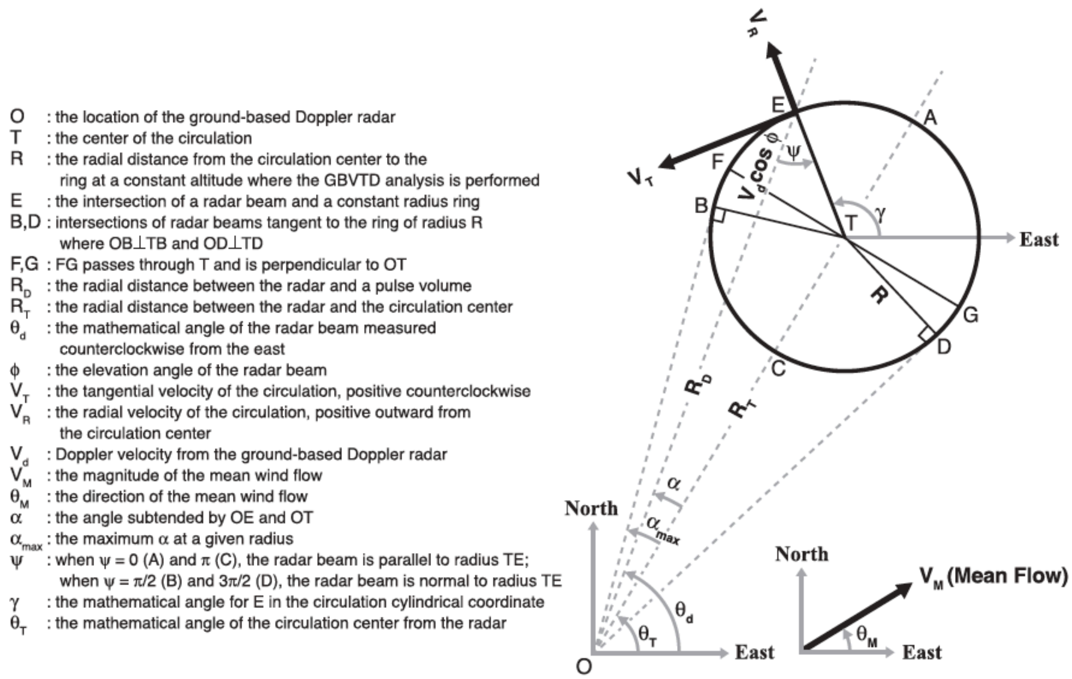


**Fig. 1: The geometry used in a GBVTD analysis. Based on a figure from Lee et al. (1999)**

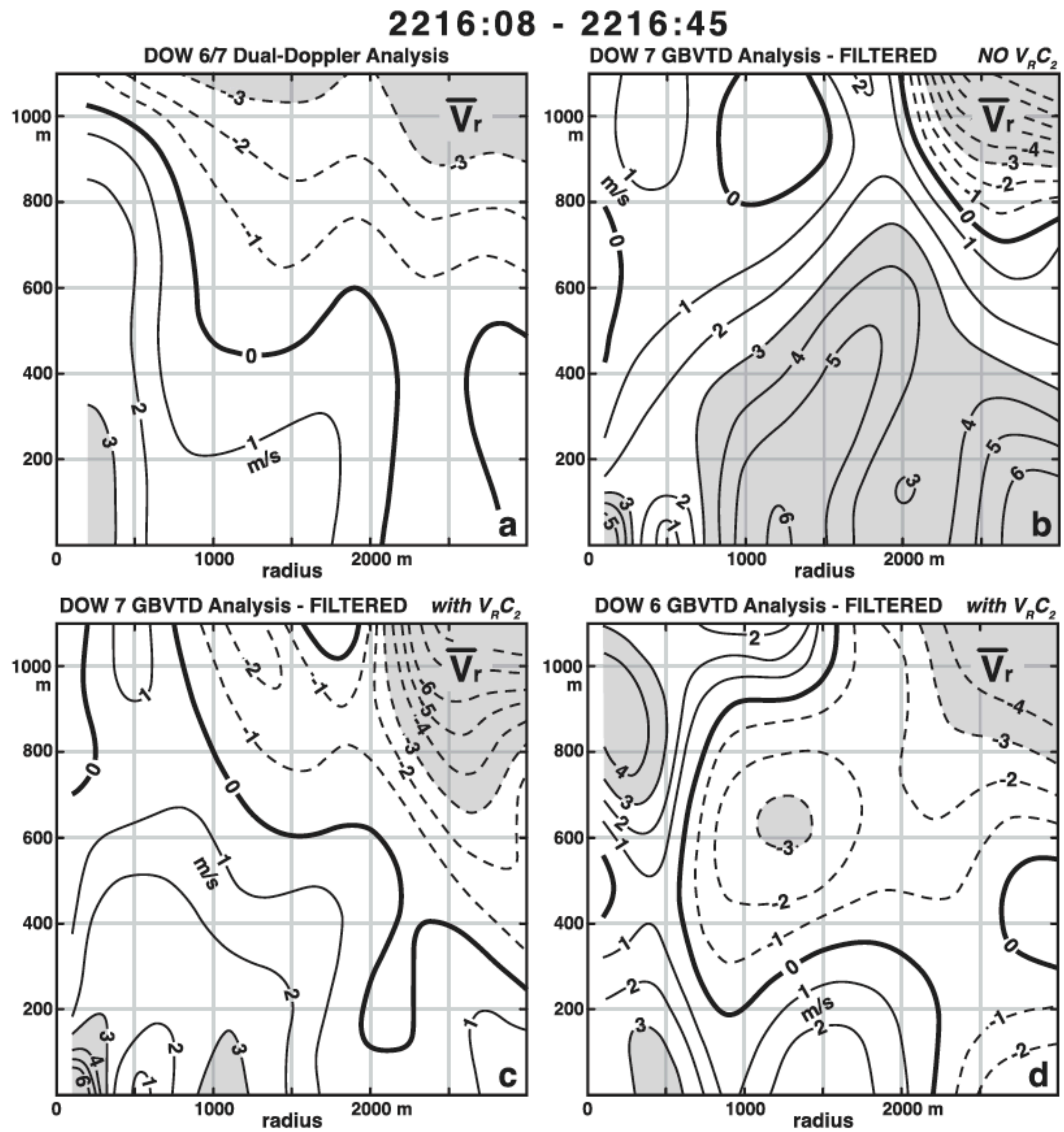


**Fig. 2 Range-height cross section of the axisymmetric radial velocities for 2216:08-2216:45 UTC for the LaGrange tornado. (a) Based on the azimuthally averaged dual-Doppler wind synthesis using data collected by DOW6 and DOW7. (b) Based on a GBVTD analysis using data collected by DOW7 and filtered to resolve wavelengths similar to the dual-Doppler wind synthesis. The $V_RC_2$ term has been ignored in this calculation. (c) As in (b), but including the $V_RC_2$ term estimated from the dual-Doppler analysis. (d) As in (c), but for DOW6. Values > 3 m $s^{-1}$ or <-3 m $s^{-1}$ are shaded gray.**

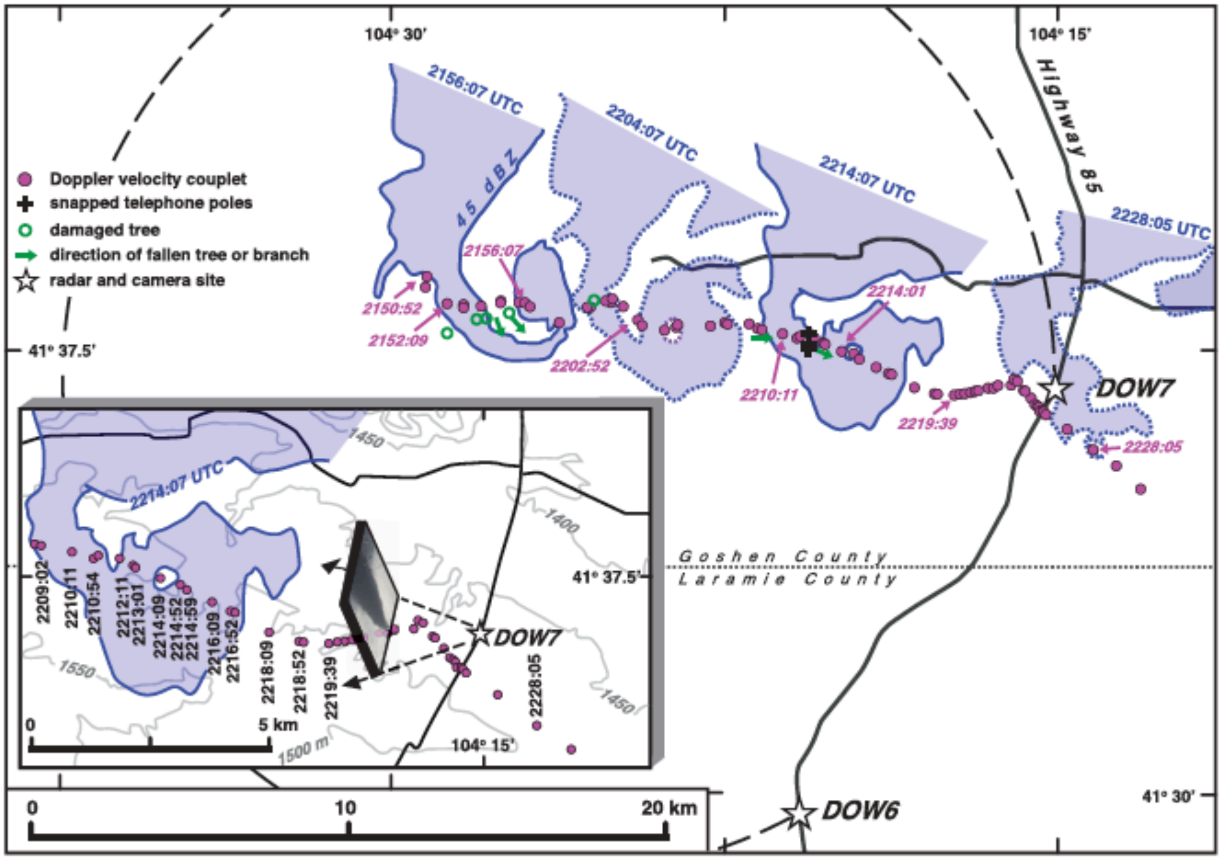

Fig. 3 Hook echo (1° elevation angle) associated with the LaGrange supercell storm at 2156:07, 2204:07,2214:07, and 2228:05 UTC recorded from the DOWs. Magenta dots represent the location of the tornadic rotational couplet based on low-level scans. Damage to telephone poles and trees are plotted (explanation of the symbols are shown in the legend). An enlargement near DOW7 is shown in the inset. The times of the rotational couplet observations are labeled on the figure. A schematic illustrating the series of photographs taken from the DOW7 site is also shown. The gray lines are the height of the topography. The locations of DOW6 and DOW7 are shown by the stars. The primary dual-Doppler lobe is plotted. The radar reflectivity values greater than 45 dBZ are shaded blue.

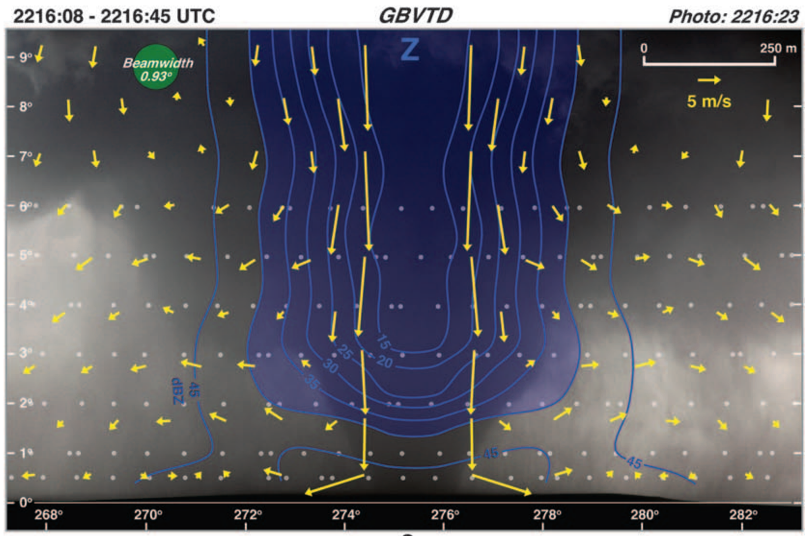
2216:08 - 2216:45 UTC
GBVTD
Photo: 2216:23
Z
Beamwidth
0.93°
0
250 m
5 m/s
dBZ
9°
8°
7°
6°
5°
4°
3°
2°
1°
0°
268°
270°
272°
274°
276°
278°
280°
282°

a

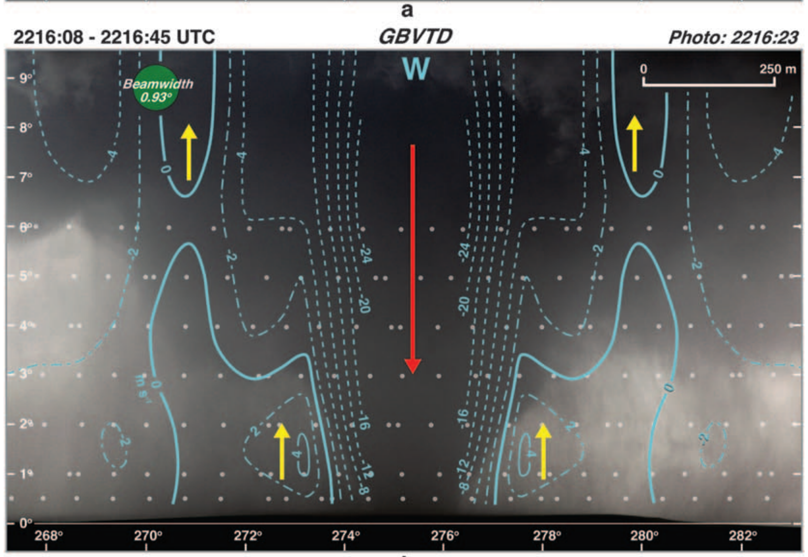
2216:08 - 2216:45 UTC
GBVTD
Photo: 2216:23
W
Beamwidth
0.93°
0
250 m
9°
8°
7°
6°
5°
4°
3°
2°
1°
0°
268°
270°
272°
274°
276°
278°
280°
282°

b

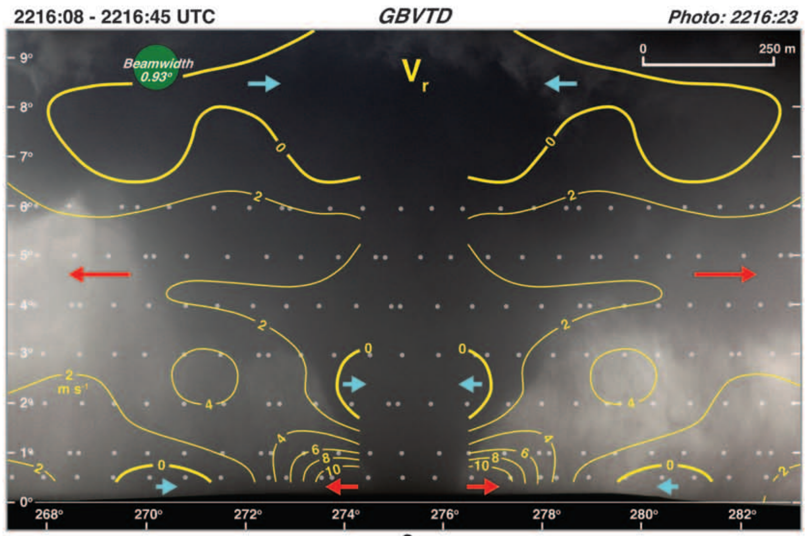
2216:08 - 2216:45 UTC
GBVTD
Photo: 2216:23
Beamwidth 0.93°
Vr
0
250 m
9°
8°
7°
6°
5°
4°
3°
2°
1°
0°
m s⁻¹
268°
270°
272°
274°
276°
278°
280°
282°

c

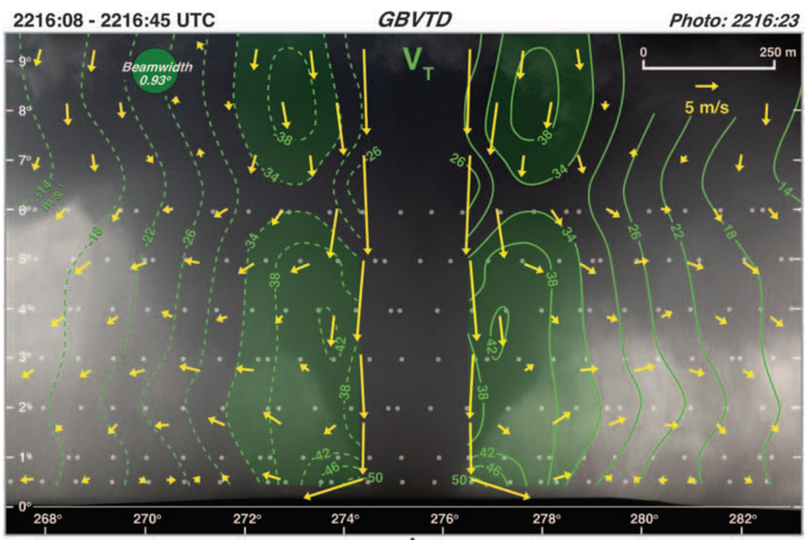
2216:08 - 2216:45 UTC
GBVTD
Photo: 2216:23
Beamwidth 0.93°
VT
0
250 m
5 m/s
9°
8°
7°
6°
5°
4°
3°
2°
1°
0°
268°
270°
272°
274°
276°
278°
280°
282°

d

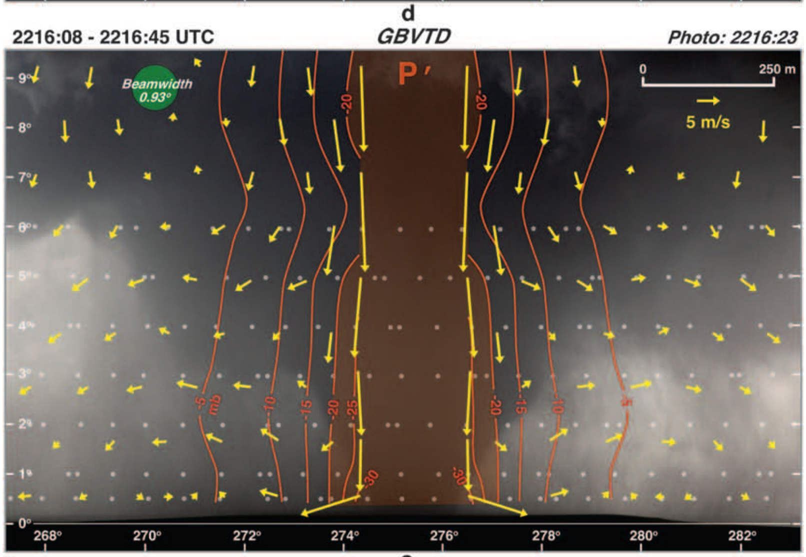
2216:08 - 2216:45 UTC
GBVTD
Photo: 2216:23
Beamwidth 0.93°
P′
0
250 m
5 m/s
mb
9°
8°
7°
6°
5°
4°
3°
2°
1°
0°
268°
270°
272°
274°
276°
278°
280°
282°

e

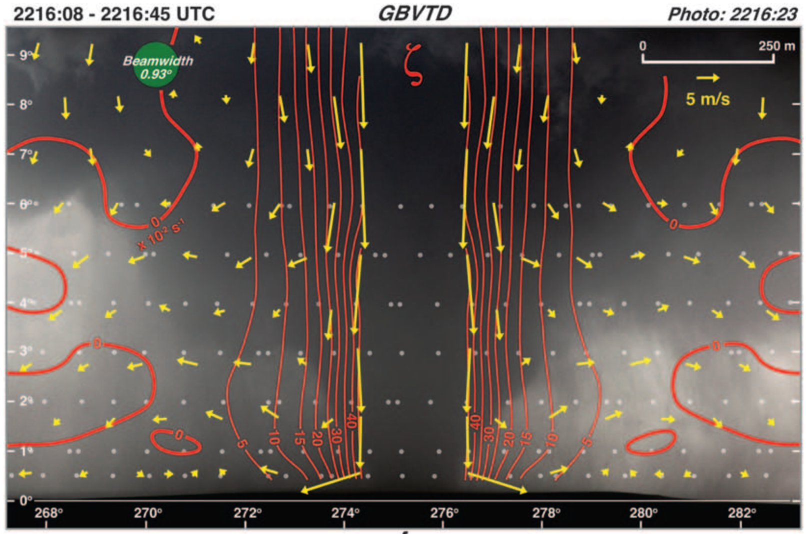


f

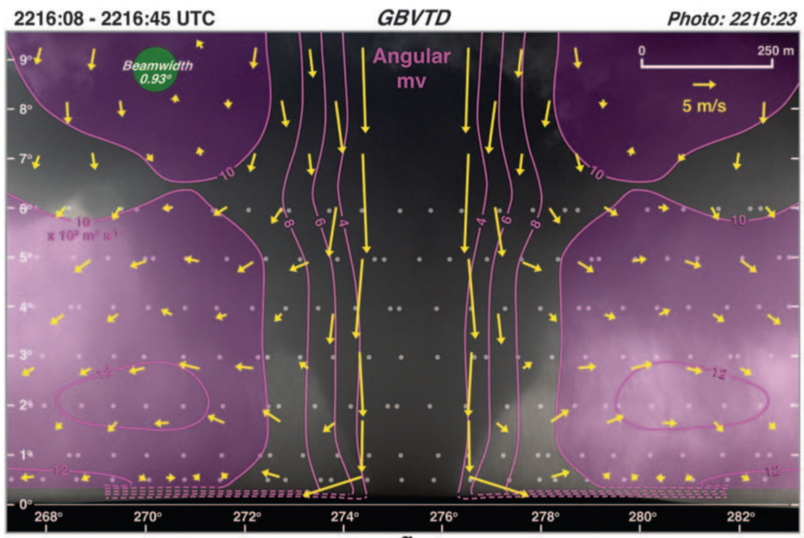


g

**Fig. 4 GBVTD analysis for the 2216:08-2216:45 UTC volume from DOW7 superimposed on top of a photograph of the LaGrange tornado at 2216:23 UTC. (a) Radar reflectivity (dBZ) and the two-dimensional wind field. Reflectivity values less than 40 dBZ are shaded. (b) Vertical velocity (m $s^{-1}$). Solid and dashed lines represent positive and negative velocities, respectively. Dash-dot contours have been added in regions with weak gradients. Red and yellow arrows denote areas of downdraft and updraft, respectively. (c) Radial velocity (m $s^{-1}$). Red and blue arrows denote areas of outflow and inflow, respectively. (d) Tangential velocities (m $s^{-1}$) and the two-dimensional wind field. Solid and dashed lines represent velocities into and out of the figure, respectively. Shaded regions represent magnitudes > 34 m $s^{-1}$. (e) Perturbation pressure (mb) and the two-dimensional wind field. Shaded region represents perturbation pressure less than -20 mb. (f) Vertical vorticity ($10^{-2}$ $s^{-1}$) and the two-dimensional wind field. (g) Angular momentum ($10^{3}$ $m^{2}$ $s^{-1}$) and the two-dimensional wind field. Shaded regions represent angular momentum greater than 10 X $10^{3}$ $m^{2}$ $s^{-1}$. Dashed isopleths of angular momentum represent an extrapolation of the analysis in a region devoid of data. The small dots represent the raw data points from DOW7 between 0.5° and 6°. The scale labeled on the figure is valid at the distance of the tornado**

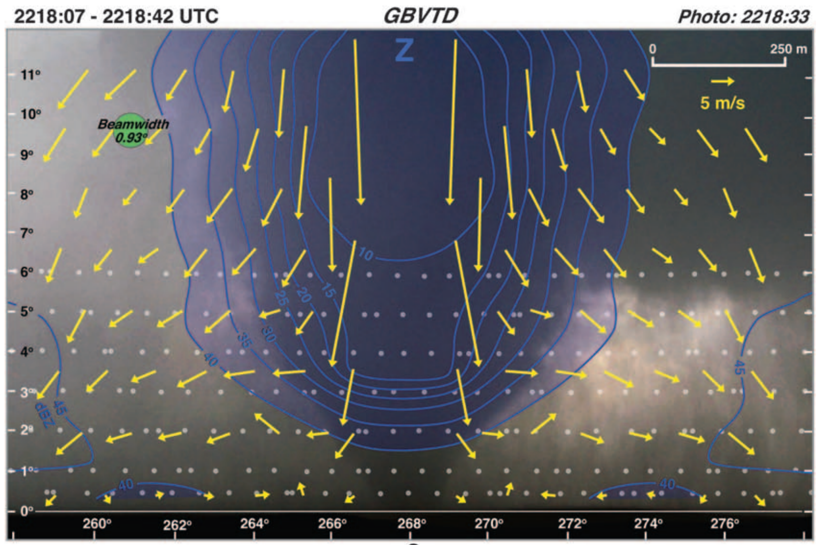

2218:07 - 2218:42 UTC
GBVTD
Photo: 2218:33
Z
0
250 m
5 m/s
Beamwidth
0.93°


a

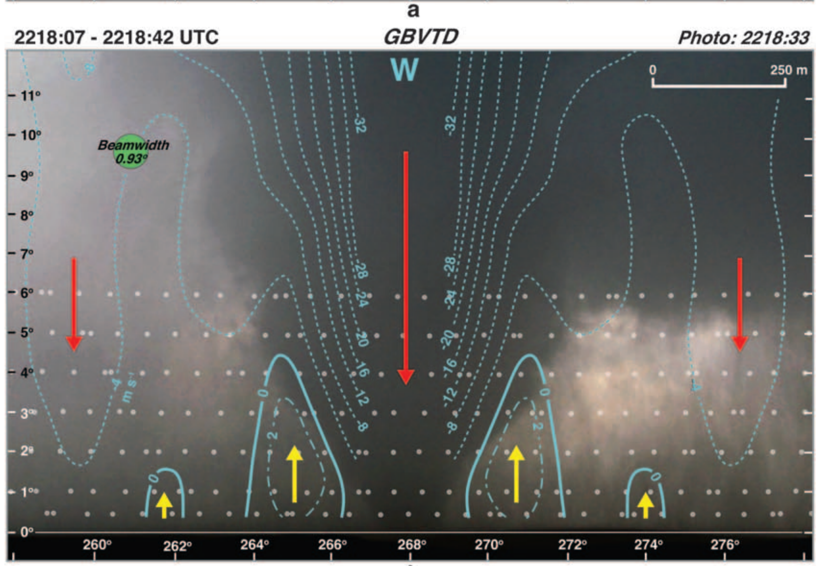

2218:07 - 2218:42 UTC
GBVTD
Photo: 2218:33
W
0
250 m
Beamwidth
0.93°


b

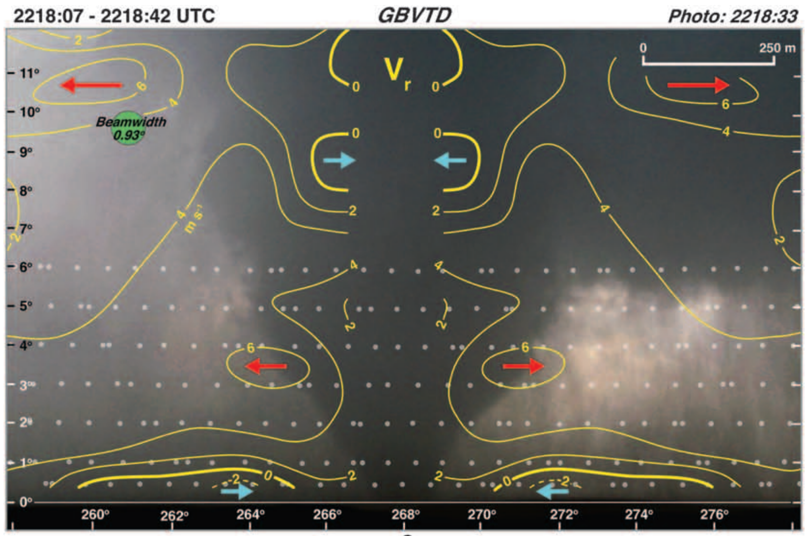

2218:07 - 2218:42 UTC
GBVTD
Photo: 2218:33
V_r
0
250 m
Beamwidth
0.93°
m s⁻¹
11°
10°
9°
8°
7°
6°
5°
4°
3°
2°
1°
0°
260°
262°
264°
266°
268°
270°
272°
274°
276°


c

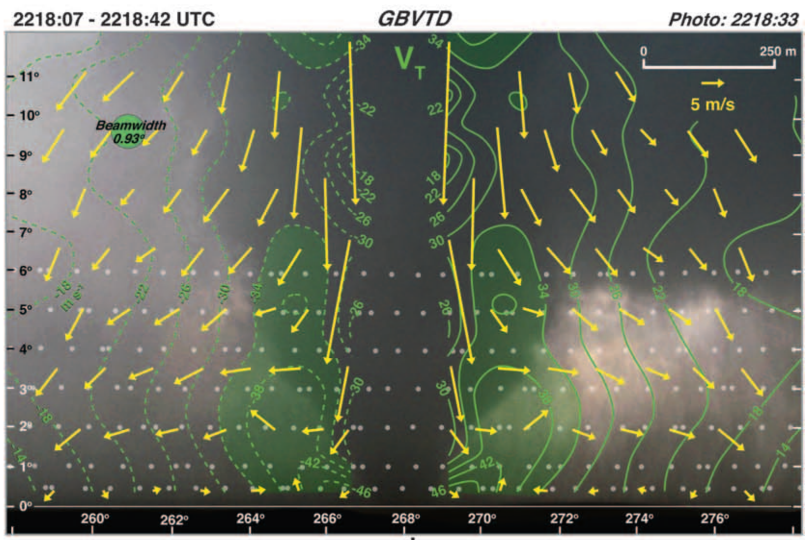

2218:07 - 2218:42 UTC
GBVTD
Photo: 2218:33
V_T
0
250 m
5 m/s
Beamwidth
0.93°
m s⁻¹
11°
10°
9°
8°
7°
6°
5°
4°
3°
2°
1°
0°
260°
262°
264°
266°
268°
270°
272°
274°
276°


d

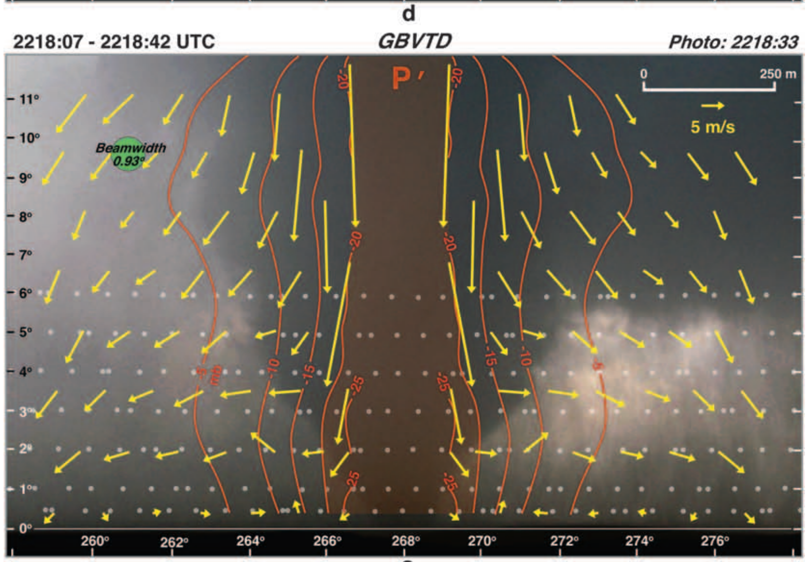

2218:07 - 2218:42 UTC
GBVTD
Photo: 2218:33
P′
0
250 m
5 m/s
Beamwidth
0.93°
11°
10°
9°
8°
7°
6°
5°
4°
3°
2°
1°
0°
260°
262°
264°
266°
268°
270°
272°
274°
276°


e

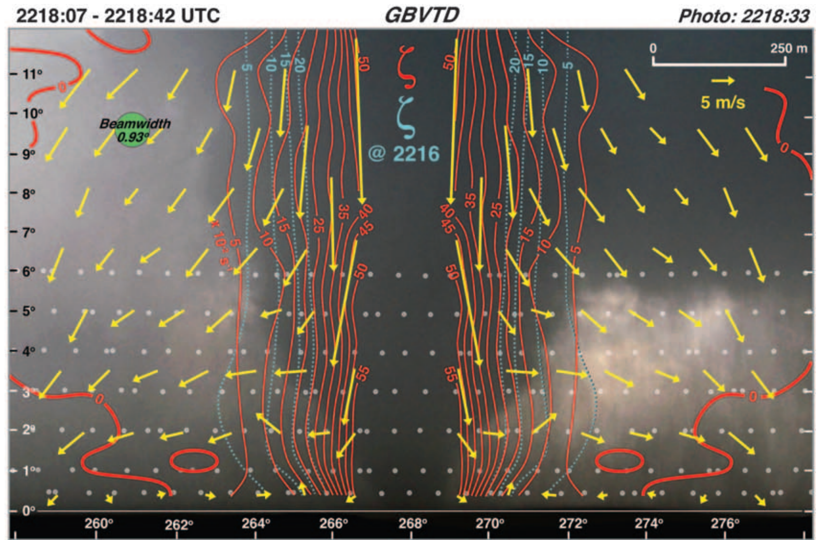


f

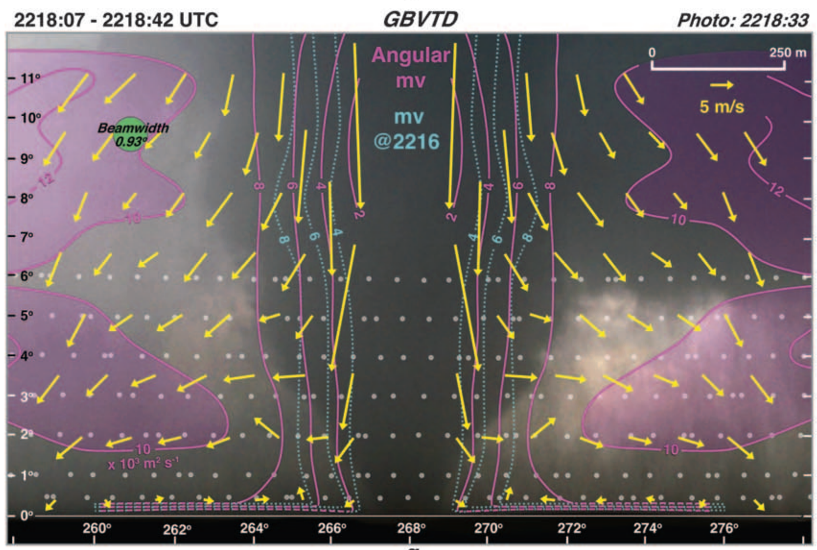


g

**Fig. 5 GBVTD analysis for the 2218:07-2218:42 UTC volume from DOW7 superimposed on top of a photograph of the LaGrange tornado at 2218:33 UTC. (a) Radar reflectivity (dBZ) and the two-dimensional wind field. Reflectivity values less than 40 dBZ are shaded. (b) Vertical velocity (m s$^{-1}$). Solid and dashed lines represent positive and negative velocities, respectively. Dash-dot contours have been added in regions with weak gradients. Red and yellow arrows denote areas of downdraft and updraft, respectively. (c) Radial velocity (m s$^{-1}$). Solid and dashed lines represent positive and negative velocities, respectively. Red and blue arrows denote areas of outflow and inflow, respectively. (d) Tangential velocity (m s$^{-1}$) and the two-dimensional wind field. Solid and dashed lines represent velocities into and out of the figure, respectively. Shaded regions represent magnitudes >34 m s$^{-1}$. (e) Perturbation pressure (mb) and the two-dimensional wind field. Shaded region represents perturbation pressure less than -20 mb. (f) Vertical vorticity (10$^{-2}$ s$^{-1}$) and the two-dimensional wind field. Representative vertical vorticity isopleths from the 2216:08-2216:45 UTC volume are plotted (light blue dotted lines). (g) Angular momentum (10$^{3}$ m$^{2}$ s$^{-1}$) and the two-dimensional wind field. Shaded regions represent angular momentum greater than 10 X 10$^{3}$ m$^{2}$ s$^{-1}$. Dashed isopleths of angular moment represent an extrapolation of the analysis in a region devoid of data. Representative angular momentum isopleths from the 2216:08-2216:45 UTC volume are plotted (light blue dotted lines). The small dots represent the raw data points from DOW7 between 0.5° and 6°. The scale labeled on the figure is valid at the distance of the tornado.**

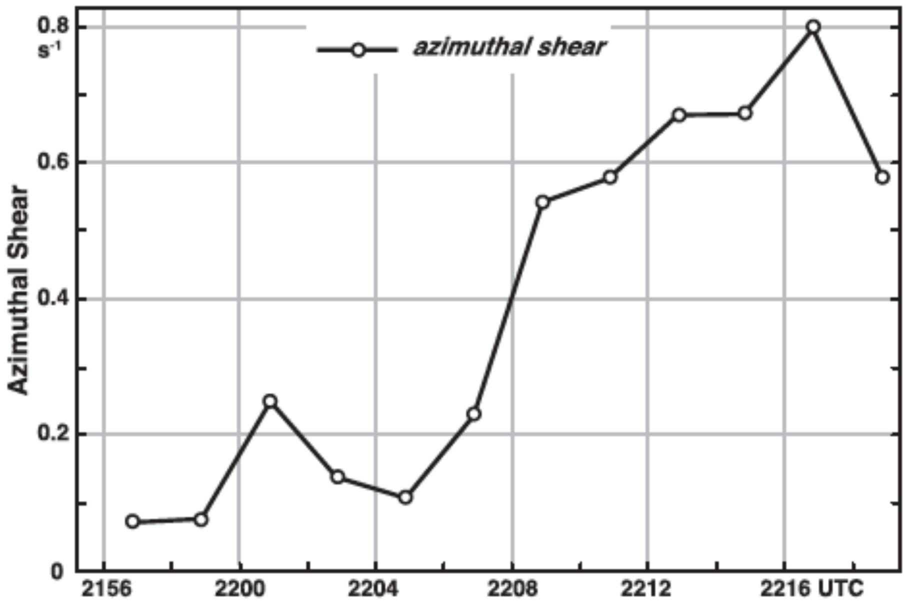


**Fig. 6 Time plot of azimuthal shear associated with the tornado based on single-Doppler velocity measurements at 0.5° from DOW7.**

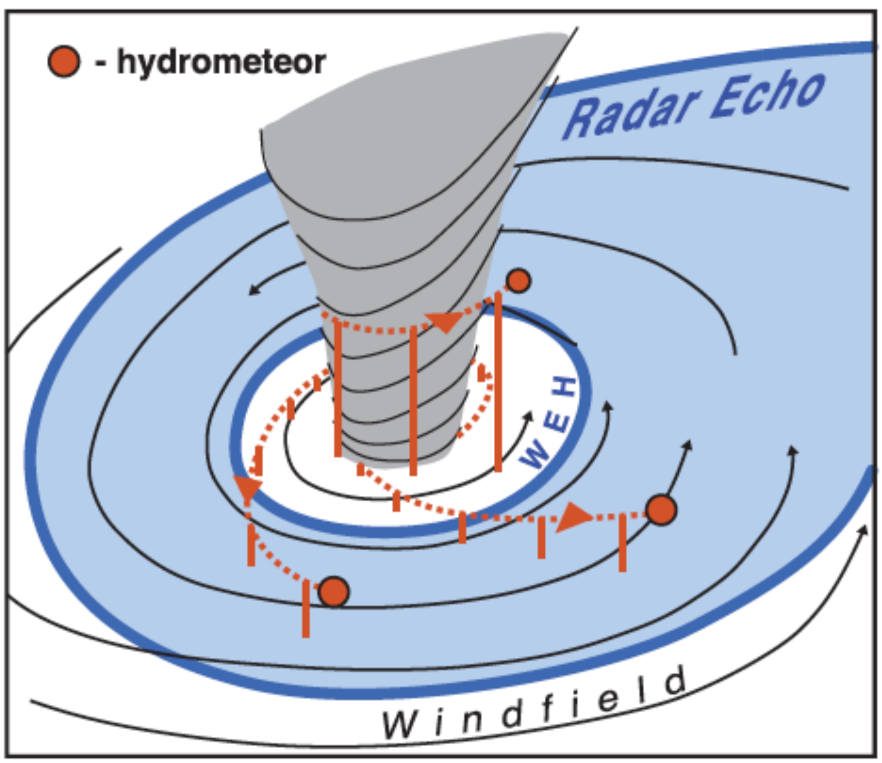


**Fig. 7 Schematic illustrating the centrifuging of hydrometeors within and near an intense tornadic circulation. Centrifuging leads to the creation of a WEH, which was larger than the funnel cloud in the current case. The figure also illustrates the difference between the wind field (black lines) and the trajectory of the hydrometeors (orange dashed lines). The latter is measured by a Doppler radar and leads to a positive bias in the derived radial velocities accompanying the tornado**

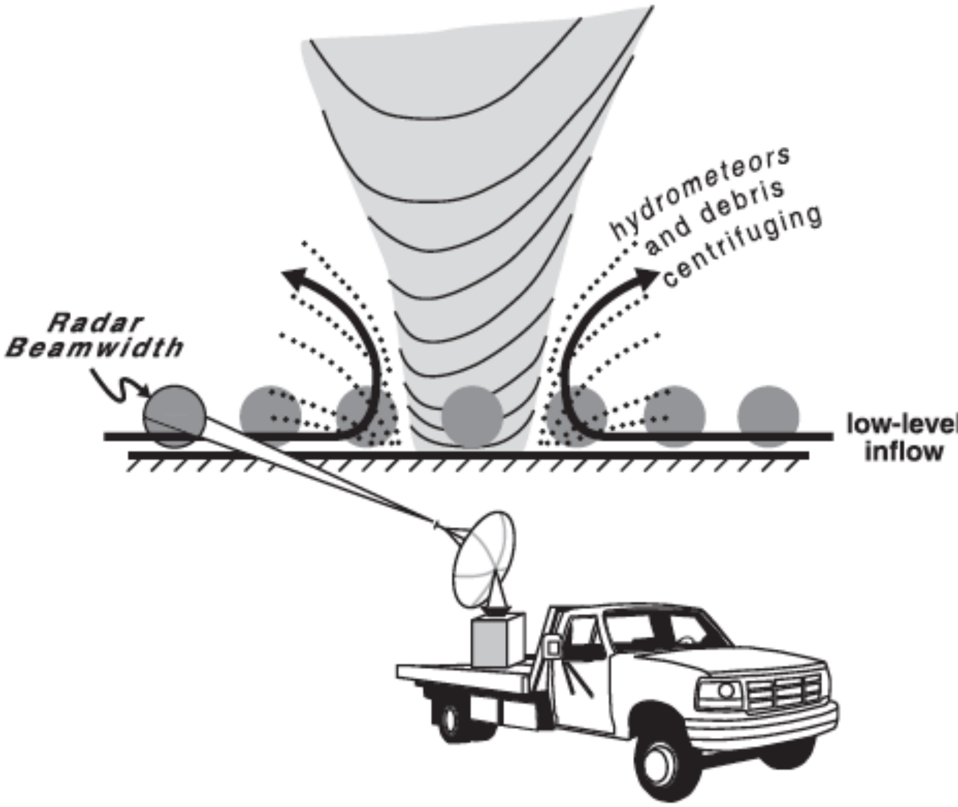


**Fig. 8 Schematic illustrating the difficulty in measuring the low-level inflow into tornadoes. Centrifuging of hydrometeors and debris results in a positive bias in the radial velocities. In addition, the challenge of scanning near the ground is shown by the inability of the radar beam to fully resolve the low-level radial inflow.**

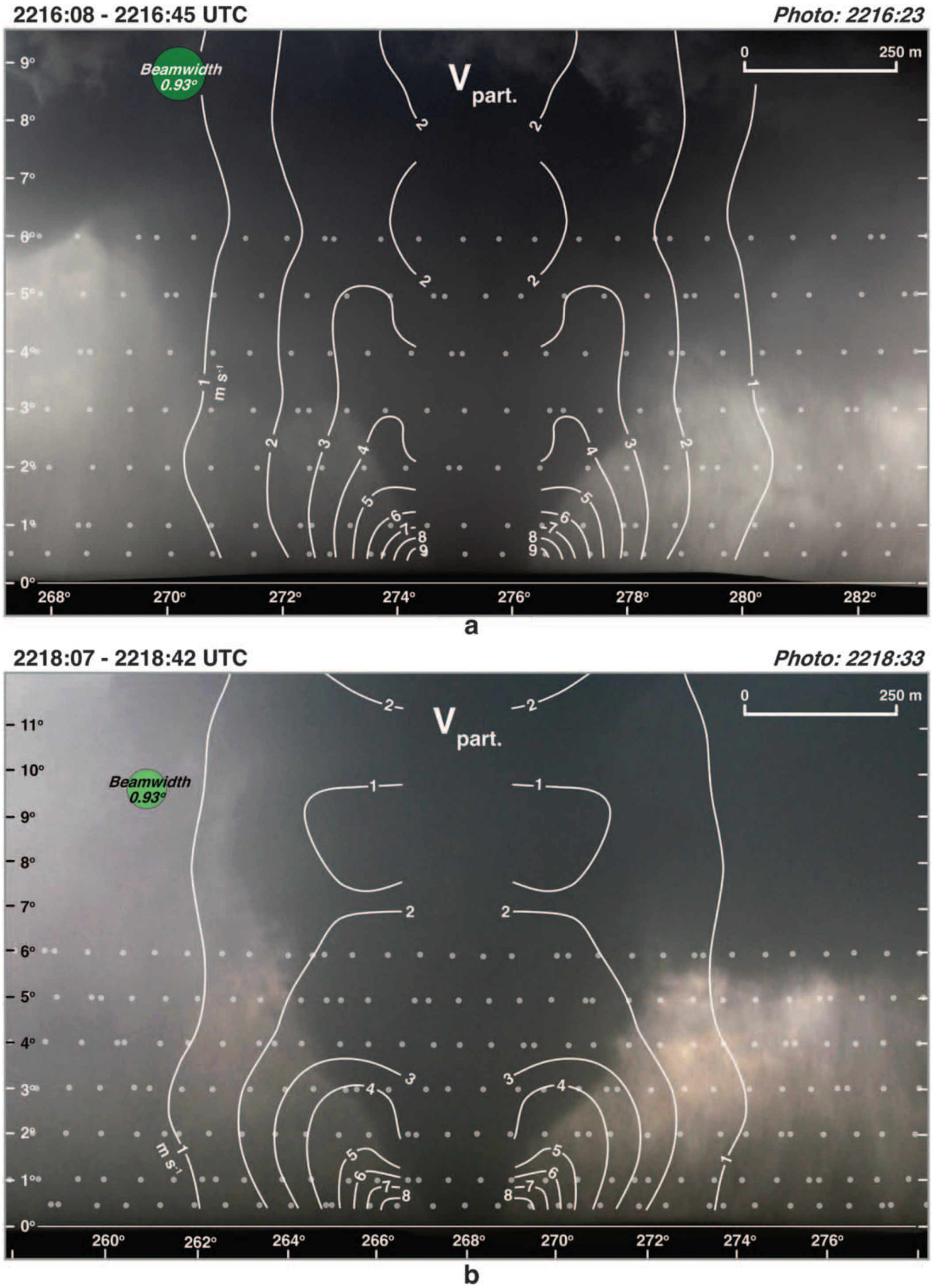


**Fig. 9 Estimate of the positive bias to the radial velocity profile owing to the centrifuging of hydrometeors for (a) 2216:08-2216:45 and (b) 2218:07-2218:42 UTC.**

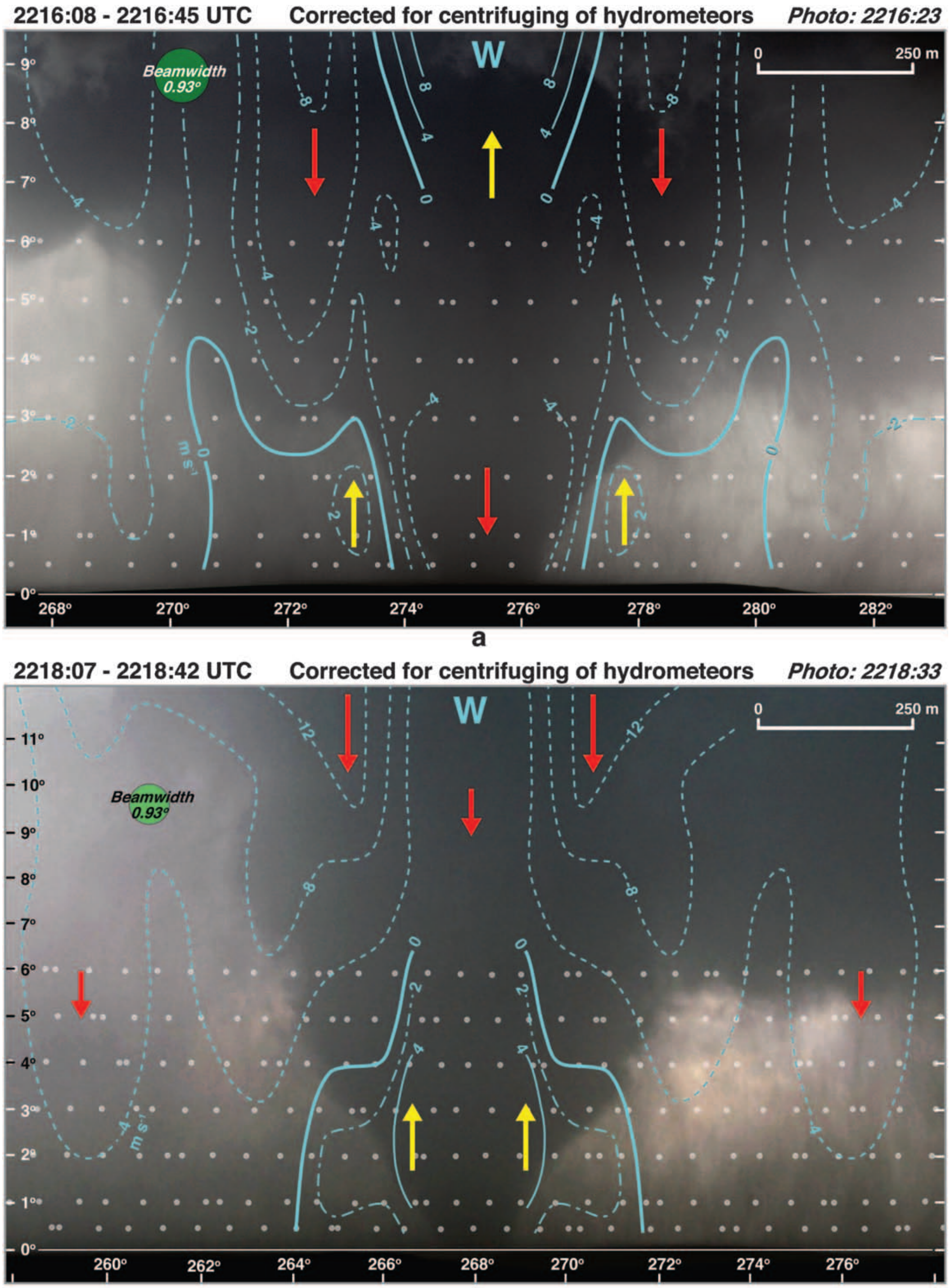


**Fig. 10 Estimate of the vertical velocities after removing the effect of centrifuging of hydrometeors for (a) 2216:08-2216:45 and (b) 2218:07-2218:42 UTC. Solid and dashed lines represent positive and negative velocities, respectively. Dash-dot contours have been added in regions with weak gradients. Red and yellow arrows denote areas of downdraft and updraft, respectively.**

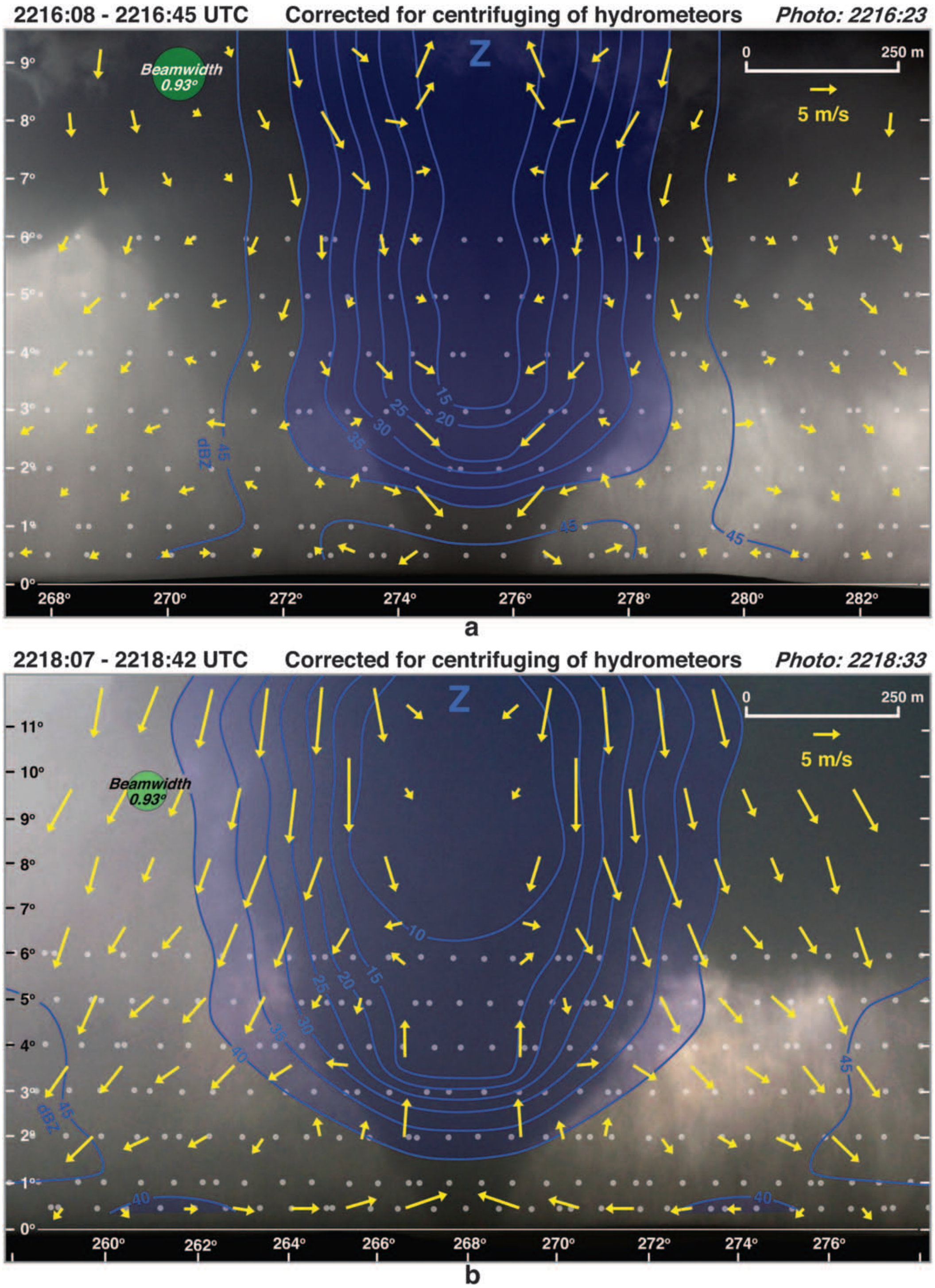


**Fig. 11 Radar reflectivity and an estimate of the two-dimensional wind field after removing the effect of centrifuging of hydrometeors for (a) 2216:08-2216:45 and (b) 2218:07-2218:42 UTC. Radar reflectivities shaded blue are less than 40 dBZ.**